JOURNAL OF SPACECRAFT AND ROCKETS
Vol. 44, No. 2, March–April 2007

Direct Simulation Monte Carlo Simulations of Ballute Aerothermodynamics Under Hypersonic Rarefied Conditions

James N. Moss*
NASA Langley Research Center, Hampton, Virginia 23681-2199

DOI: 10.2514/1.22706

This paper presents computational results obtained with the direct simulation Monte Carlo method for towed ballute applications. A ballute is an inflatable drag device that can be used to create a large amount of drag at high altitudes. Consequently, ballutes provide a potential technology for achieving aerocapture when the primary spacecraft velocity reduction (ΔV) is achieved at much higher altitudes than with the conventional rigid aeroshell. Because the ΔV is achieved at relatively high altitudes, rarefaction can be significant and is the motivation for the current study with the direct simulation Monte Carlo method. Computed surface and flowfield results are presented for a toroidal ballute, isolated tethers when exposed to freestream flow conditions, and the flow interactions resulting from a toroidal ballute when towed by a 6 m diameter Mars Pathfinder shaped (without tethers) spacecraft. All results presented are for Earth entry at velocities of 14 to 7 km/s (primary focus is at 8.55 km/s, same as some previous Titan aerocapture studies) and altitudes of 200 to 100 km. Variations of drag and heating coefficients as a function of rarefaction are presented. A description of the flow structure is provided and also an explanation of how it is affected by shock interactions produced solely by the ballute and those resulting from the two body combination of towed ballute and spacecraft is also given.

Nomenclature

C_D	=	drag coefficient, drag/[$(0.5\rho_\infty V_\infty^2)$(frontal area)]
C_H	=	heat transfer coefficient, $q_w/(0.5\rho_\infty V_\infty^3)$
C_p	=	pressure coefficient, $(p_w)/(0.5\rho_\infty V_\infty^2)$
D	=	diameter, ring diameter of toroid, maximum diameter of spacecraft, m
D_{cs}	=	cross-sectional diameter of toroid, m
$Kn_{\infty,L}$	=	freestream Knudsen number, λ_∞/L
L	=	separation length, characteristic length, m
n	=	number density, m^{-3}
p	=	pressure, N/m^2
q	=	wall heat transfer rate, W/m^2
R	=	ring radius of toroid, m
R_i	=	inside radius of toroid, m
R_o	=	outside radius of toroid, m
s	=	distance along the surface, m
T	=	temperature, K
V_∞	=	freestream velocity, m/s
X	=	mole fractions
x, y	=	model coordinates, m
λ_∞	=	mean free path in freestream, m
ρ	=	density, kg/m^3
σ	=	surface emissivity
τ	=	viscous shear stress, N/m^2

Subscripts

R	=	rotational temperature
T	=	translational temperature
V	=	vibrational temperature
W	=	wall
∞	=	freestream

Presented as Paper 4949 at the 38th Thermophysics Conference, Toronto, Ontario, Canada, 6–9 June 2005; received 24 January 2006; revision received 20 March 2006; accepted for publication 22 March 2006.

*Senior Research Engineer, Aerothermodynamics Branch, Mail Stop 408A; j.n.moss@larc.nasa.gov. Fellow AIAA.

I. Introduction

THE ballute (balloon + parachute) is an inflatable structure used to increase the drag of the vehicle to which it is attached. The ballute concept was first studied [1,2] for hypersonic applications in the late sixties as a potential means of assisting the Viking landers during Mars entry. More recent studies [3–5] have focused on possible applications of this technology for flight in planetary atmospheres during entry and aerocapture. A significant advantage of using a ballute is that the peak aerodynamic deceleration and heating experienced by a spacecraft occurs at much lower densities (higher altitudes) than would be the case without the ballute. Consequently, the lander or orbiter is subject to less severe heating and aerodynamic forces during its atmospheric encounter. Because of the ballute's large size relative to the payload, the convective heating rates will be much smaller for the ballute than the vehicle payload. The ballute heating will have to be accommodated by the ballute through conduction and radiation at temperatures below 770–870 K if lightweight materials [3,5] such as Kapton or Polyboxoxazole (PBO), respectively, are used.

Recent studies [4–9] have focused on the towed inflatable structures as potential technology for enabling aerocapture maneuvers of spacecraft at planets and atmospheric bearing moons such as Titan. The ballute provides most of the drag force and energy dissipation during the maneuver and is detached once the desired velocity change has been achieved. Trajectory studies for four candidate missions are discussed in [4], where it is demonstrated that the timing of ballute detachment provides sufficient trajectory modulation capability to enable aerocapture despite atmospheric uncertainties and navigation errors at the target planet. Although the system studies show the concept to be plausible, substantial development work is necessary to verify key assumptions and quantify performance levels. Aerothermodynamic simulations, both experimental and computational, are essential elements in the overall assessment activities.

The current study is made for flight conditions in the Earth's atmosphere while accounting for reacting chemistry and nonequilibrium viscous effects, effects that have a major impact on a complex flow structure characterized by shock interactions, recirculation, and potential unsteady effects. Computations are made by using the DS2V code of Bird [10,11], a time accurate direct simulation Monte Carlo (DSMC) program that provides 2-D/axisymmetric simulation capabilities. The current simulations are for

both isolated and towed toroidal ballutes in the Earth's atmosphere at altitudes of 200–100 km and for freestream velocities of 7– 14 km/s (primary focus of 8.55 km/s). The baseline toroidal geometry (52-m ring diameter with a 13-m cross-sectional diameter) is one that has been used in previous ballute mission aerocapture design studies [6–9] for the Titan Organics Explorer mission, that is, a toroid with an inside radius of 19.5 m and an outside radius of 32.5 m. Individual or isolated simulations are made for the toroidal ballute, a 6-m diameter spacecraft (enlarged Mars Pathfinder), and different size tethers. Next, interacting simulations are made for the combination of spacecraft and ballute (without tethers) where the spacecraft wake passes inside the ballute with negligible influence on it. The final simulations are made for a ballute with a smaller baseline ring diameter (26 m) configured such that the spacecraft's wake bow shock impinges on the ballute and produces augmented heating and pressure loads on the ballute. The spacecraft-ballute shock interactions are also accompanied by a large recirculation region that extends upstream and impinges on the spacecraft afterbody and produces a significant increase in the spacecraft's afterbody heating and pressure. This large recirculation region is shown to be unstable initially, but after a long simulation time, the flow becomes steady.

II. DSMC Program and Model Parameters

The DSMC program used in the current study is the DS2V program of Bird [10,11], a general 2-D/axisymmetric code that provides both time accurate unsteady flow and time-averaged steady flow simulations. Molecular collisions are simulated with the variable hard sphere molecular model. The Larsen–Borgnakke statistical model [12] controls the energy exchange between kinetic and internal modes. For the present study, the simulations are performed by using a five-species reacting air gas model while considering energy exchange between translational, rotational, and vibrational modes. The molecular gas constants used in the current study are those given in [10]. Also, a rotational relaxation collision number of 5 and a temperature dependent vibrational collision number [Eq. (6.53) of [10]] were used. More details regarding the DS2V code can be found in [13], and examples of recent validation studies are presented in [13–15].

For all simulations, the model surface is assumed to be noncatalytic and at a radiative equilibrium wall temperature calculated by using the local surface energy transfer and a surface emissivity of 0.8. Furthermore, a minimum surface temperature was specified at each altitude that ranged from 200 to 300 K. As for gas-surface interactions, they are assumed to be diffuse, with full energy accommodation except for the vibrational mode, in which the surface accommodation is assumed to be 0.2.

An indicator of the resolution achieved in a given simulation is given by the ratio of the mean collision separation between collision partners to the local mean free path (mcs/mfp). For blunt body flows, as considered herein, the average value for this parameter over the computational domain should be less than 0.1 to ensure that the local values of (mcs/mfp) are less than 1 adjacent to the surface. If these guidelines are not met, the calculated heating rates will be on the high side.

III. Results

Figure 1 presents a schematic of a towed ballute, highlighting the three elements for which computations are made using the DSMC method: that is, a spacecraft (an enlarged Mars Pathfinder) with the dimensions shown in Fig. 2, tethers which are analyzed at freestream conditions, and a towed toroidal ballute. Calculations are made for both isolated ballutes and towed ballutes. The freestream atmospheric conditions [16] (for an exospheric temperature of 1200 K), including the freestream mole fractions, are listed in Table 1. Figure 3 shows the present density–velocity parameters considered and how they relate to a Titan Explorer trajectory (a smaller ballute than used in the present study—with diameters of 24/6 m rather than the present 52/13 m) discussed in [4]. As described in [4], the sharp corner in the lower right-hand part of the velocity vs density plot is the point of ballute detachment, after which, the speed changes little as the spacecraft climbs out of the

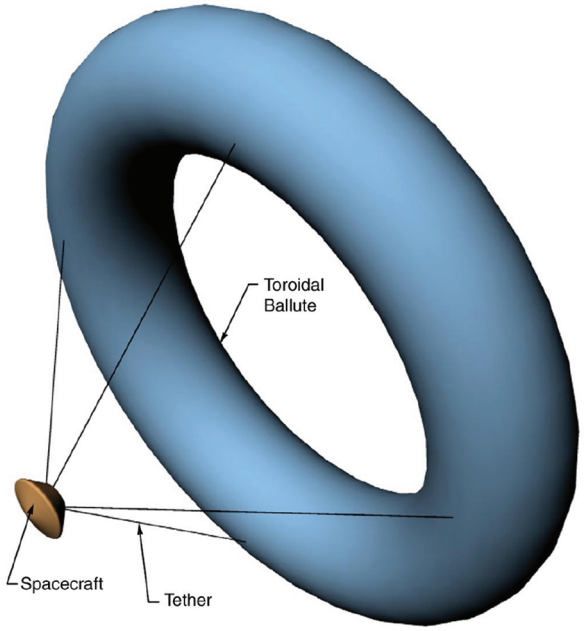

Fig. 1 Schematic of a toroidal ballute towed behind a spacecraft.

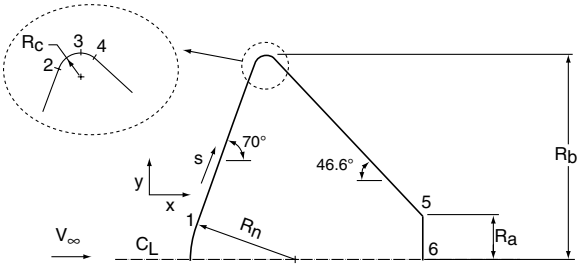

Location	x	y	s
1	0.0906	0.5140	0.5246
2	0.9595	2.9013	3.0651
3	1.1005	3.0000	3.2484
4	1.2095	2.9531	3.3704
5	3.4098	0.6263	6.5728
6	3.4098	0.0000	7.1990

$R_n = 1.503$
$R_c = 0.150$
$R_a = 0.626$
$R_b = 3.0$

Dimensions in m

Fig. 2 Spacecraft configuration—enlarged Mars Pathfinder.

Table 1 Freestream conditions

Altitude, km	λ_∞, m	n_∞, m^{-3}	ρ_∞, kg/m^3	T_∞, K	X_{O_2}	X_{N_2}	X_O
200	389.90	8.9996×10^{15}	3.2830×10^{-10}	1026	0.0315	0.4548	0.5138
140	20.79	9.3526×10^{16}	3.8548×10^{-9}	625	0.0618	0.6517	0.2865
120	3.03	5.2128×10^{17}	2.2642×10^{-8}	368	0.0845	0.7327	0.1828
110	0.64	2.1246×10^{18}	9.6068×10^{-8}	247	0.1232	0.7704	0.1064
105	0.26	4.9759×10^{18}	2.3004×10^{-7}	211	0.1528	0.7819	0.0653
100	0.10	1.1898×10^{19}	5.5824×10^{-7}	194	0.1768	0.7844	0.0388

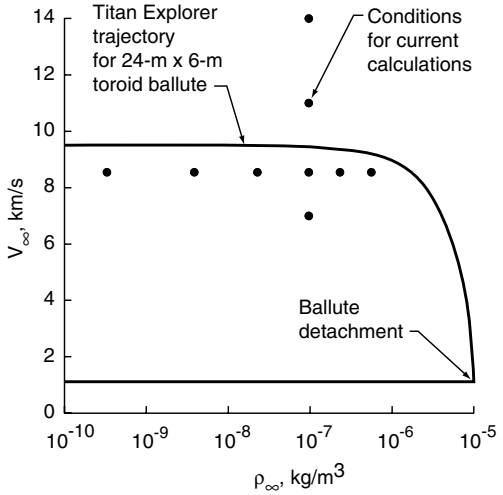

Fig. 3 Freestream density and velocity values used in the present study and a Titan Explorer aerocapture trajectory from [4].

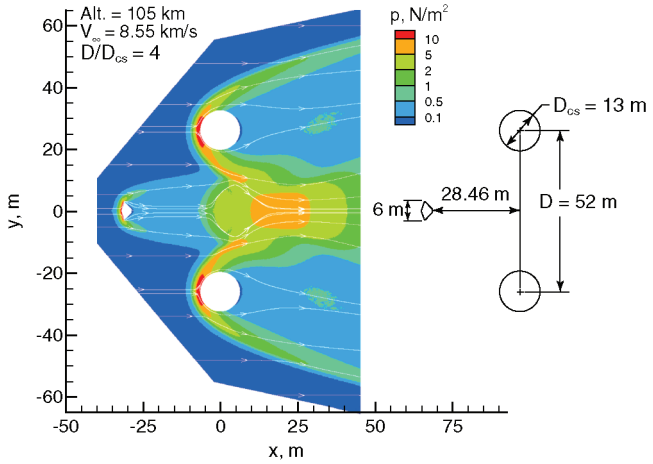

Fig. 4 Pressure contours and streamlines for the baseline configuration (toroidal ballute with a ring diameter D equal to 52 m and a cross-sectional diameter D_{cs} equal to 13 m).

atmosphere and achieves an aerocapture orbit. With a much larger ballute, as used in the current study, the velocity depletion would occur at even lower densities than those for the trajectory presented in Fig. 3.

The computed pressure contours and streamlines for the current baseline spacecraft and towed toroidal ballute configuration are shown in Fig. 4 for an altitude of 105 km at a freestream velocity of 8.55 km/s. Also shown in Fig. 4 are the overall spatial dimensions for the towed ballute. The separation distance between the aft end of the spacecraft and the center of the ballute is 28.46 m. For this baseline configuration, the wake of the spacecraft passes inside the ballute without altering the ballute's surface distribution for heating rate, pressure, or shear stress with respect to that for the isolated ballute (without the towing spacecraft). As will be discussed later, the reverse flow region present in the current simulation is not present for the isolated ballute simulations.

Tables 2–6 present results for the maximum values of surface heating rate, pressure, and radiative equilibrium wall temperature experienced by isolated elements of a towed system, that is, values experienced by the ballute, spacecraft, and tethers. With the exception of the tether calculations, results are also included for the drag and various coefficients as a function of altitude (rarefaction), velocity, and ballute configuration (ratio of ring diameter to a fixed, cross-sectional diameter such that the ratio of the two diameters are 4, 3, and 2). This section will conclude with results for a tandem spacecraft and ballute, for both the baseline configuration and for a geometric configuration, in which the flow becomes unstable initially due to the positioning of the shock interactions such that the wake bow shock impinges directly on the ballute.

A. Impact of Toroid Geometry on Flow Interactions and Surface Loads for Isolated Toroidal Ballutes at 105-km Altitude

As discussed in [5,6], the flow through the core of the toroidal ballute exhibits strong self-interactions due to the convergence of the bow shocks. The self-interactions are strongly affected by both the flow conditions and the toroidal geometry. This section presents results of simulations for constant freestream flow conditions in which the toroidal geometry is varied such that the ratio of the ring diameter to a fixed, cross-sectional diameter (13 m) includes values of 4, 3, and 2. The effect of varying the geometry is demonstrated in Figs. 5–9 on both surface distributions and flow structure for reacting air at a 105-km altitude and a freestream velocity of 8.55 km/s. The surface distributions for heating rate, pressure, skin friction, and radiative equilibrium wall temperature (Figs. 5 and 6) show negligible effect when the diameter ratio is reduced from 4 to 3, but a very noticeable effect is evident when the ratio is further reduced from 3 to 2, producing additional asymmetry in the distributions and a significant reduction in the maximum heating rate. Table 3 provides a summary of the global and local quantities in both dimensional and coefficient form.

The impact of the geometry variations on the flow structure is more obvious, as demonstrated in Figs. 7–9, in which calculated pressure

Table 2 Aerodynamic, heating, and radiative equilibrium wall temperature results for a ballute at a freestream velocity of 8.55 km/s

Altitude, km	Drag, N	C_D	p, N/m^2	C_p	q, W/m^2	C_H	T_W, K
200	52	2.04	0.025	2.08	100	0.975	217
140	587	1.96	0.29	2.06	1,020	0.847	388
120	3,138	1.78	1.70	2.05	4,400	0.622	560
110	11,300	1.52	6.85	1.95	9,300	0.310	670
105	25,020	1.40	16.1	1.92	12,000	0.167	720
100	57,360	1.32	39.0	1.91	14,500	0.083	750

Table 3 Aerodynamic, heating, and radiative equilibrium wall temperature results for different ballute configurations at a freestream velocity of 8.55 km/s and an altitude of 105 km

Ballute diameters, m	Frontal area, m^2	Drag, N	C_D	p, N/m^2	C_p	q, W/m^2	C_H	T_W, K
52/13	2123.7	25,020	1.40	16.1	1.92	12,000	0.167	720
39/13	1592.8	18,750	1.40	16.2	1.93	12,300	0.171	720
26/13	1061.9	12,820	1.44	16.3	1.94	8,850	0.123	665

Table 4 Aerodynamic, heating, and radiative equilibrium wall temperature results for a ballute at an altitude of 110 km

Velocity, km/s	Drag, N	C_D	p, N/m^2	C_p	q, W/m^2	C_H	T_W, K
7.00	7,529	1.51	4.60	1.95	5,400	0.328	585
8.55	11,300	1.52	6.85	1.95	9,300	0.310	670
11.0	18,880	1.53	11.4	1.96	19,800	0.310	810
14.0	31,181	1.56	18.6	1.98	48,000	0.364	1020

Table 5 Aerodynamic, heating, and radiative equilibrium wall temperature results for an enlarged Mars Pathfinder at a freestream velocity of 8.55 km/s

Altitude, km	Drag, N	C_D	p, N/m^2	C_p	q, W/m^2	C_H	T_W, K
105	419.4	1.76	16.8	2.00	36,000	0.501	940
100	962.0	1.67	40.0	1.96	59,000	0.338	1075

Table 6 Heating and radiative equilibrium wall temperature results for tethers at 45 deg to freestream velocity of 8.55 km/s

Altitude, km	Diameter, m	$Kn_{\infty,D}$	q, W/m^2	T_W, K
110	0.010	64	21,000	822
110	0.001	640	21,000	822
100	0.010	10	115,000	1260
100	0.001	100	121,000	1280

contours and streamlines are presented for diameter ratios of 4, 3, and 2, respectively. As seen in these figures, the shock layer thickness directly in front of the toroid ring is of the same order as the toroid cross-section radius. For a diameter ratio of 4, peak static pressure (almost 50 N/m^2) occurs along the axis and 17 m aft of the toroid's center. As the size of the hole in the toroid decreases, the peak pressure along the axis decreases and moves forward: there is a magnitude of 17 N/m^2 and 5.1 m aft of the toroid's center for a diameter ratio of 3 and a magnitude of 14.5 N/m^2 and 7 m in front of the toroid's center for a diameter ratio of 2. For the later case, the shock is essentially normal to the axis, with the peak static pressure located in front of the toroid. Even though the peak heating rate is less for the smaller diameter ratio, it is probably not a desired configuration because the experimental study of Rasheed et al. [9] shows that the flow becomes unstable for a towed toroidal ballute when a flat disk blocks the ballute's hole. Also, as discussed later, a ballute with a diameter ratio of 2 is shown to be unstable initially for the same separation distance between spacecraft and toroidal ballute as shown in Fig. 4.

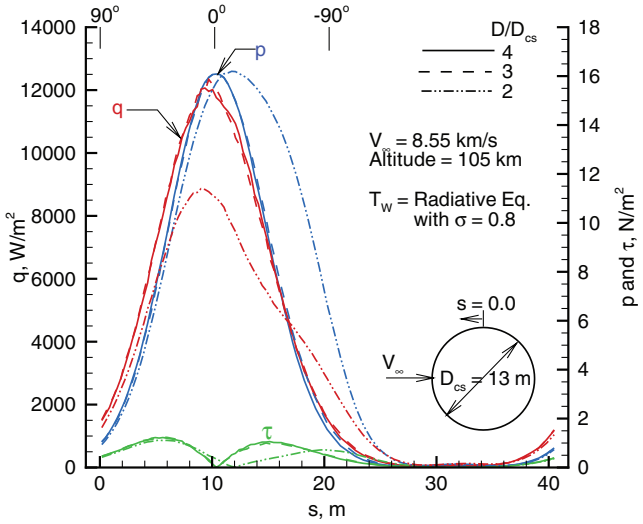

Fig. 5 Effect of varying ballute ring diameter on surface heating rate, pressure, and skin friction.

An indication of the thermal environment of a ballute at 105-km altitude and a freestream velocity of 8.55 km/s is presented in Fig. 10. Shown are the overall kinetic temperature (weighted average [10] of translational, rotational, and vibrational temperatures) contours for an isolated toroidal ballute. The maximum overall kinetic temperature for this case is approximately 18,000 K and

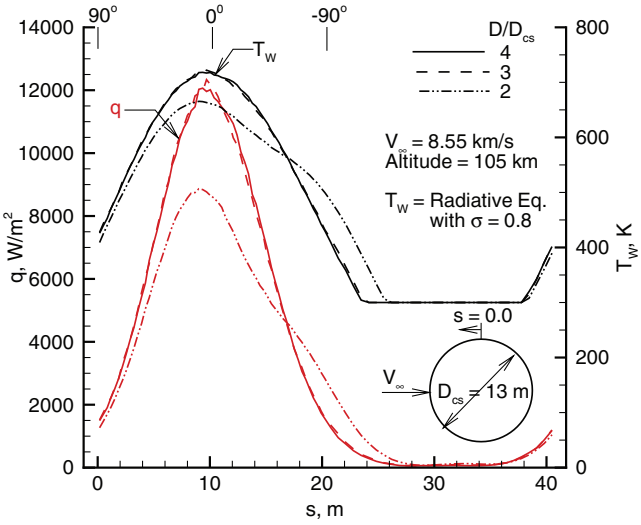

Fig. 6 Effect of varying ballute ring diameter D on surface heating rate and radiative equilibrium wall temperature.

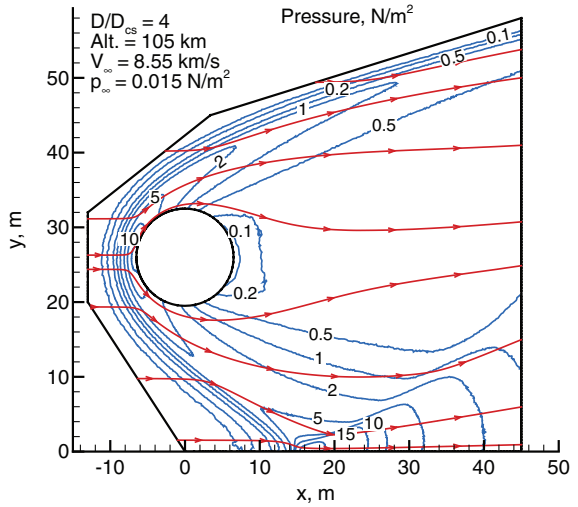

Fig. 7 Pressure contours and streamlines for 105-km altitude, velocity = 8.55 km/s, and $D/D_{cs} = 4$.

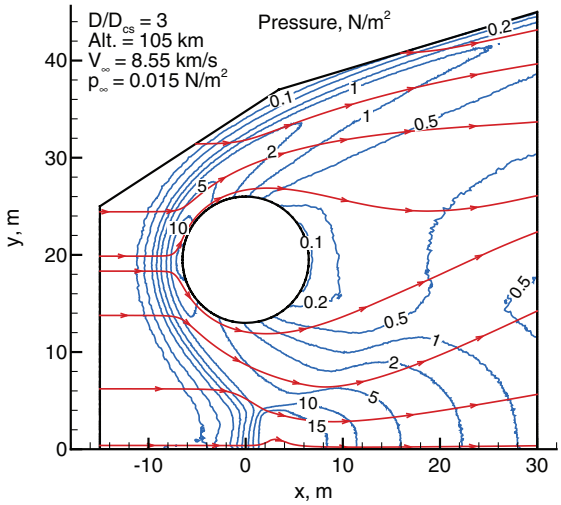

Fig. 8 Pressure contours and streamlines for 105-km altitude, velocity = 8.55 km/s, and $D/D_{cs} = 3$.

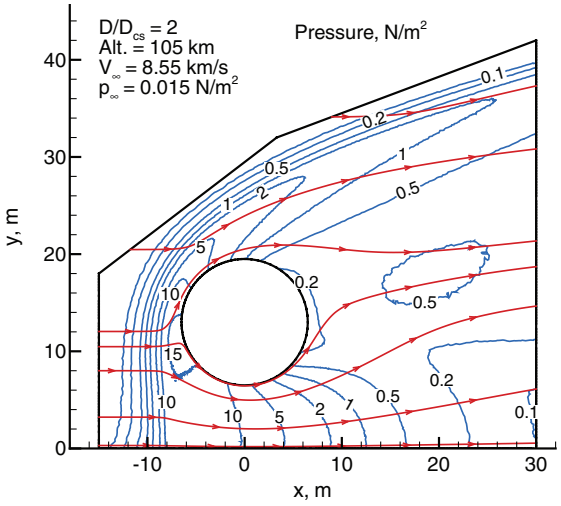

Fig. 9 Pressure contours and streamlines for 105 km altitude, velocity = 8.55 km/s, and $D/D_{cs} = 2$.

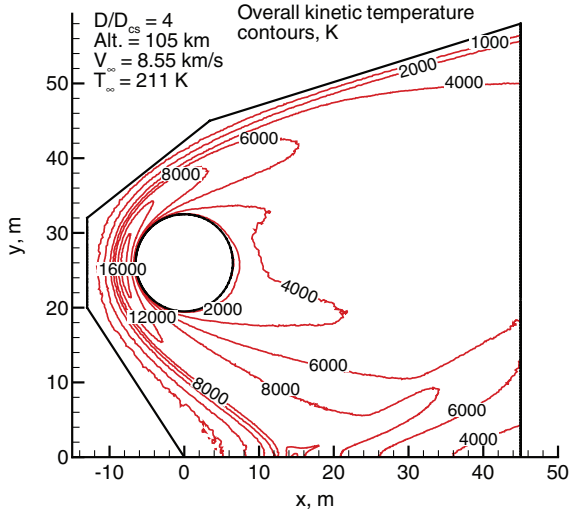

Fig. 10 Temperature contours for 105 km altitude, velocity = 8.55 km/s, and $D/D_{cs} = 4$.

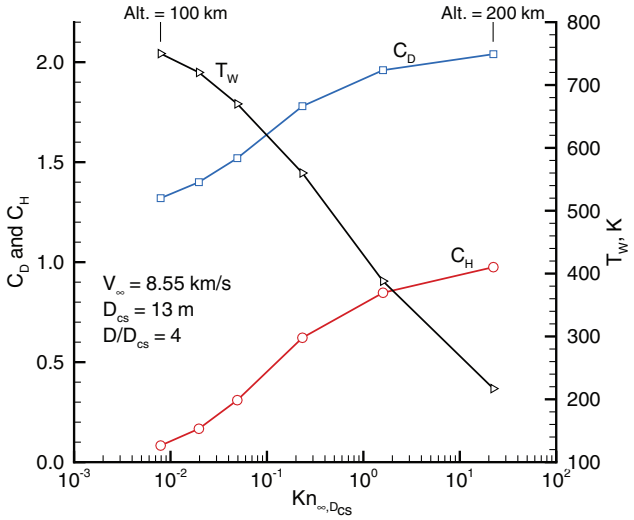

Fig. 11 Effect of rarefaction on ballute drag coefficient, forebody stagnation point heating rate coefficient, and radiative equilibrium wall temperature.

occurs both in front of the ballute and in the shock interaction region along the axis. Thermal nonequilibrium is significant because the maximum translational temperature is approximately 24,000 K, the maximum rotational temperature is 15,000 K, and the maximum vibrational temperature is 8000 K. The extent of chemical dissociation is significant for this case because the number of species striking the surface is predominantly that from three chemical species —atomic nitrogen, molecular nitrogen, and atomic oxygen—listed in the order of decreasing surface flux. With this high level of dissociation (oxygen is complete), it is obvious that if the ballute's surface promotes atomic recombinations, then the surface heating rates would be higher than the values presented herein where a noncatalytic surface assumption has been used.

B. Impact of Rarefaction on Isolated Toroidal Ballutes

Table 2 provides a summary of both global and forebody stagnation quantities (drag, pressure, heating rate, and radiative equilibrium wall temperature) as a function of altitude (rarefaction) for a constant freestream velocity of 8.55 km/s and an isolated toroidal ballute with $D = 52$ m and $D_{cs} = 13$ m. Figure 11 presents the coefficient and wall temperature results plotted as a function of the freestream Knudsen number, in which the characteristic length used to define the Knudsen number is the toroid cross-sectional diameter. As demonstrated in Fig. 11, the coefficients approach their maximum values as the free molecular conditions are approached (Knudsen numbers on the order of 100), demonstrating that a larger percentage of the freestream momentum and energy is imparted to the ballute as the free molecular condition is approached; however, obviously the dimensional quantities decrease with increasing rarefaction. The current results show that the drag coefficient decreases substantially with decreasing rarefaction (altitude); the drag coefficient at 100 km is 65% of the value at 200 km, a result that has not been included in some of the early trajectory studies [3,4] that used a constant value for the drag coefficient.

The convective heating rate and radiative equilibrium wall temperature distributions for altitudes of 120, 110, and 100 km are presented in Fig. 12. For the wall temperature calculation, a minimum temperature was arbitrarily specified for each altitude, ranging from 250 to 300 K for these three conditions. The maximum calculated ballute surface temperature was 750 K, a value that is within the temperature limits [3] of some of the potential ballute materials such as Kapton.

C. Impact of Freestream Velocity on Isolated Toroidal Ballutes

Because the convective heating rate is proportional to the freestream velocity raised to approximately the third power, the heating rate is a very strong function of velocity. This strong relationship between velocity and heating rate is demonstrated in Fig. 13 and Table 4, in which the velocity is parametrically varied

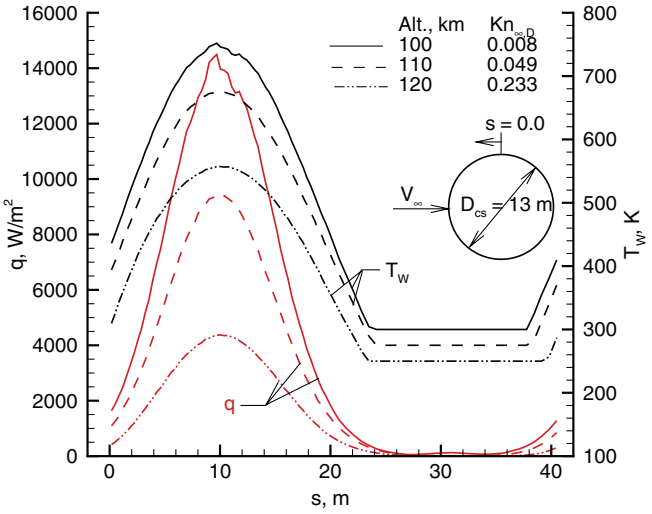

Fig. 12 Effect of rarefaction on ballute heating rate and radiative equilibrium wall temperature for a freestream velocity = 8.55 km/s and $D/D_{cs} = 4$.

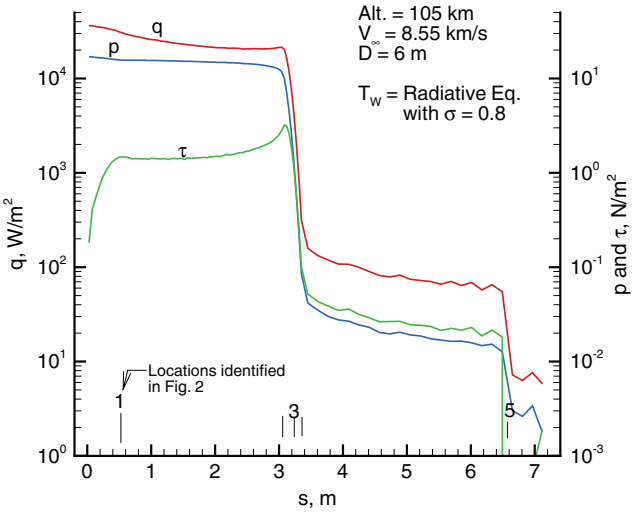

Fig. 14 Heating rate, pressure, and shear stress distribution for an enlarged Mars Pathfinder.

between 7 and 14 km/s for an isolated ballute at an altitude of 110 km. When the freestream velocity is doubled (7–14 km/s), the calculated heating rate increases by a factor of 8.9, and the maximum radiative equilibrium surface temperature increases from 585 to 1020 K, reaching temperatures that are in excess of the limits for the lightweight ballute materials previously mentioned. As shown in Table 4, the drag coefficient and stagnation point pressure and heating rate coefficients are relatively insensitive to the velocity variations.

The current calculations are deficient at the higher velocity conditions in that ionization and thermal radiation effects have not been included. Also, for the higher velocity conditions, essentially all the gas in the shock layer is dissociated before it impacts the surface. For the 14 km/s calculation, for example, 98% of the gas species that impact the surface in the forebody stagnation region are atomic species (78% atomic nitrogen and 20% atomic oxygen). For the higher velocity flow environments and for situations where the ballute surface material/s promote species recombination, then the convective heating rates would be substantially increased with respect to the present noncatalytic results.

D. Surface Results for an Enlarged Mars Pathfinder Spacecraft

For the two lower altitudes considered (105 and 100 km), Figs. 14–16 present information concerning the surface distributions for heating rate, pressure, shear stress, velocity slip, temperature jump (both translational and rotational), and radiative equilibrium wall temperature for an enlarged Mars Pathfinder (maximum body diameter equal to 6 m, see Fig. 2). Table 5 includes both the dimensional and coefficient values for drag and maximum values for pressure, heating rate, and radiative equilibrium wall temperature. With the nose radius of the spacecraft being much smaller than the cross-sectional radius of the ballute (1.5 vs 6.5 m), the maximum heating rate and wall temperature values are noticeably higher for the spacecraft (heating rate is 3 times higher at 105 km). As shown in Fig. 14 for the 105-km altitude condition, the aerodynamic loads and heating rates along the afterbody of the spacecraft are very small compared to the forebody results, 2 or more orders of magnitude less than the forebody results. The large reductions in loads and heating values occur during the expansion about the outer corner radius (locations 2–4 as identified in Fig. 2). A comparison of the heating rates and radiative equilibrium wall temperature for 105- and 100-km altitudes is presented in Fig. 15 where it is seen that the minimum specified wall temperature of 300 K is reached near $s = 3.37$ (location 4 as shown in Fig. 2).

The present heating rate distributions for the 105-km altitude case, when compared to related results obtained with Navier–Stokes calculations (Fig. 6 of [7]) show two significant differences. First, is the nature of the heating rate distribution as the flow approaches the outer corner radius expansion, where the Navier–Stokes solution

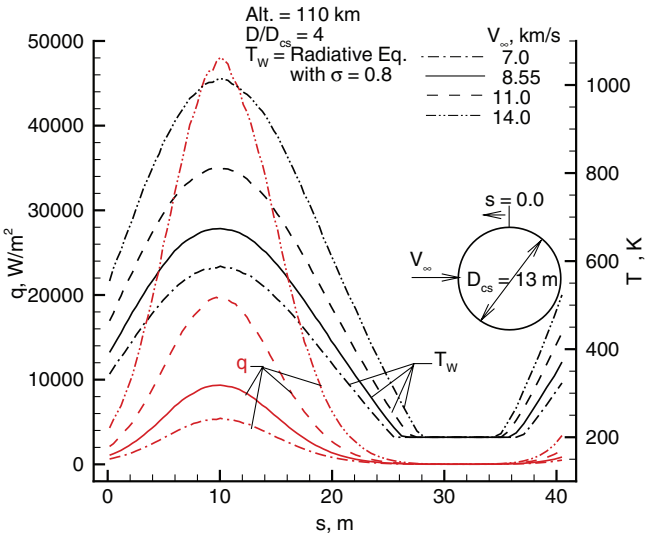

Fig. 13 Effect of freestream velocity on ballute heating rate and radiative equilibrium wall temperature for an altitude of 110 km.

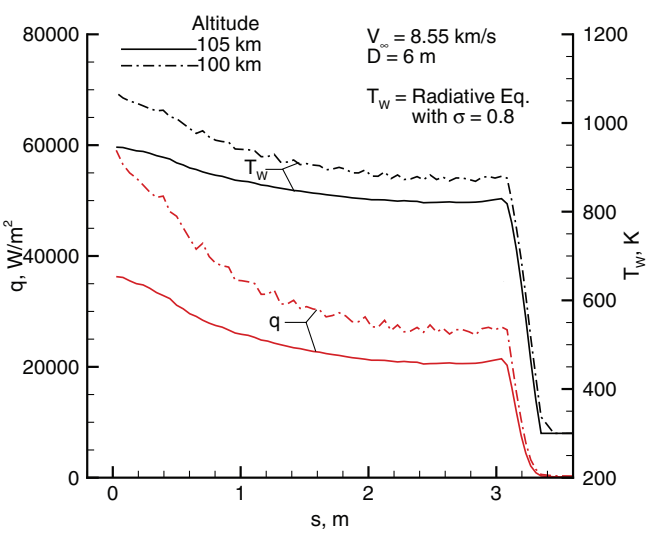

Fig. 15 Heating rate and radiative equilibrium wall temperature distributions for an enlarged Mars Pathfinder.

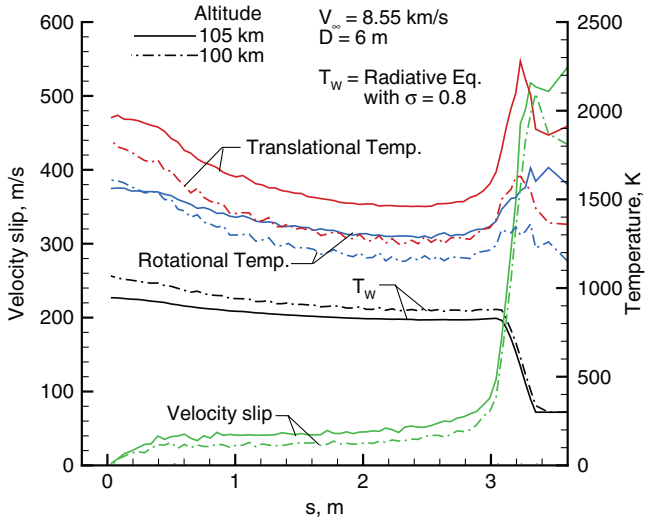

Fig. 16 Velocity slip and temperature jump (translational and vibrational) for an enlarged Mars Pathfinder.

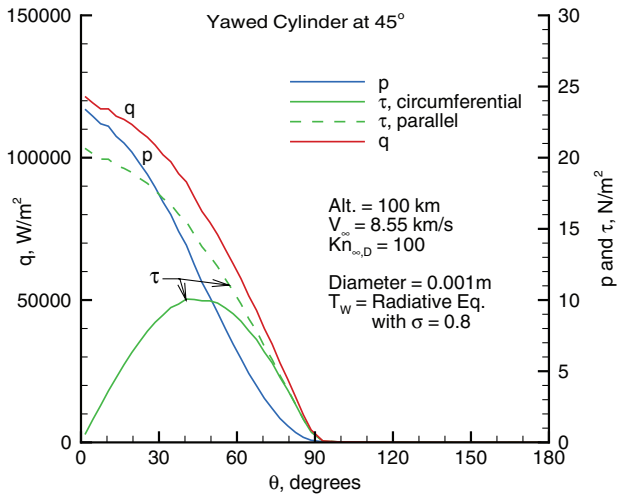

Fig. 17 Tether heating rate, pressure, and shear stress distributions (1-mm diameter yawed cylinder at 45 deg).

predicts a heating rate value that is larger than the forebody stagnation point value; however, the current DSMC solution predicts only a modest increase in heating rate as the outer corner expansion is approached, with a value much lower than the forebody stagnation point value. The second significant difference occurs for the magnitude of the heating along the spacecraft afterbody where the Navier–Stokes minimum value is approximately 2000 W/m^2; yet, the DSMC values are 100 W/m^2 or less (more than an order of magnitude difference). A potential explanation for these differences is given in Fig. 16 in which the velocity slip [velocity of gas at the surface—see Eq. (1) of [14] for the expression used to calculate the slip velocity], surface values for translational and rotational temperatures, and radiative equilibrium temperatures are presented. The differences in the gas temperature at the surface and the surface temperature is the temperature jump. As shown in Fig. 16, the temperature jump and particularly the velocity slip increase significantly as the corner expansion is approached. Also, large values for slip and temperature jump persist in the afterbody region, indicating that significant rarefaction effects are present in the corner expansion and afterbody regions, as expected.

E. Surface Results for Tethers—Yawed Cylinders at 45 deg

Of the three individual elements analyzed in the current study, tethers are the smallest and, consequently, experience the highest heating rates and radiative equilibrium surface temperatures. Results obtained for the tether simulations are summarized in Table 6 and Figs. 17 and 18. The simulations were made using the 2-D option of the DS2V code and the feature [11] of imposing a "normal-to-plane velocity" such that a surface moves in its own plane in the direction normal to the plane of the flow (circumferential direction in the case of an axially symmetric flow). Results were generated for altitudes of 110 and 100 km at a freestream velocity of 8.55 km/s. The tether was assumed to be a yawed cylinder oriented at 45 deg to the freestream. Cylinder diameters of 1 mm and 1 cm were considered, and for such small objects at high altitudes, the flow is highly rarefied. The fact that the surface distributions of the 1-mm and 1-cm tethers are the same at 110 km is just an indication that they are completely in free molecular flow. However, for the 100-km altitude conditions, the maximum heating rate (Table 6) for the larger cylinder is 95% of the corresponding 1-mm cylinder, indicating that the larger cylinder is no longer at free molecular conditions (Knudsen number of 10 rather 100 for the smaller cylinder).

The surface distributions for heating rate, pressure, and shear stress are presented in Fig. 17 for the 1-mm diameter yawed cylinder at a 100-km altitude. Shear stress distributions for both the circumferential and parallel directions are shown, accounting for the combined effects of freestream normal and parallel velocity

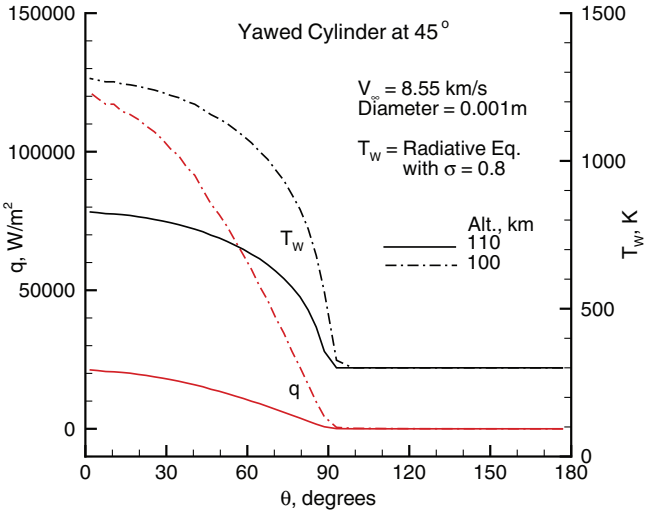

Fig. 18 Tether heating rate and radiative equilibrium wall temperature distributions (1-mm diameter yawed cylinder at 45 deg).

components. The surface distributions for the 1-cm diameter tether are the same as for the smaller tether for the 110-km conditions. Figure 18 shows the 1-mm diameter tether heating rate and wall temperature distributions for altitudes of 110 and 100 km at a constant velocity. An imposed minimum surface temperature of 300 K was used. For the lower altitude conditions considered at 8.55 km/s, tethers could be at temperatures well in excess of 1000 K based on the assumptions of the present calculations. Note that in addition to the string tethers considered here, larger column tethers are being investigated [5] as potential options in which the column tethers are likely to be inflated tubes of the same material as the ballute.

F. Toroidal Ballute when Towed Behind a Spacecraft

Previous sections have described the flow features and surface environment for individual elements of a towed ballute. This section will summarize the results of numerical simulations for the towed ballute while neglecting the presence of the tethers. The baseline geometry (see Fig. 4) is used where the toroidal ring diameter is 52 m, the ballute cross-section diameter is 13 m ($D/D_{cs} = 4$), and the separation distance between the ballute and enlarged Mars Pathfinder is 28.46 m. The freestream velocity is 8.55 km/s, and calculations were made for the altitudes listed in Table 1 between 140 to 100 km. For this altitude range, the simulations show that the wake of the 6-m

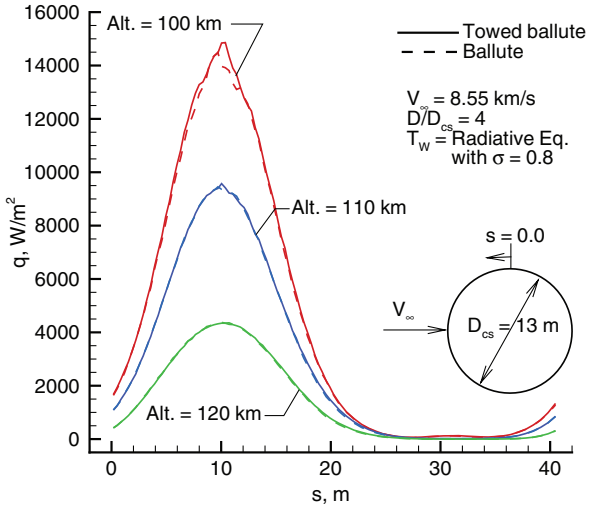

Fig. 19 Effect of a towing spacecraft (6-m diameter Mars Pathfinder) on ballute heating rate distributions.

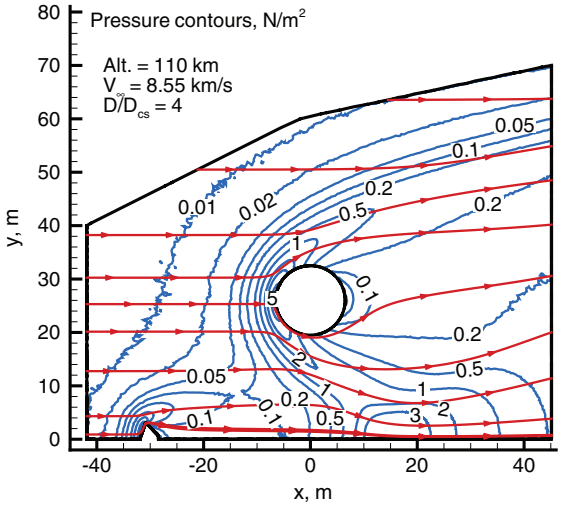

Fig. 21 Pressure contours and streamlines for a towed ballute at 110-km altitude.

diameter spacecraft has negligible impact on the ballute when compared to the ballute results when exposed to uniform freestream conditions. These findings are demonstrated in Fig. 19 where the heating rate distributions for the towed ballute (solid line) are compared with the corresponding ballute results (dashed line) for uniform freestream flow at altitudes of 120, 110, and 100 km. A similar agreement is evident (not shown) for the pressure and shear stress distributions and, consequently, the drag. These findings are not unexpected because the wake of the spacecraft passes nicely through the hole of the ballute for this particular ballute-spacecraft configuration ($D/D_{cs} = 4$ and $L = 28.46$ m).

Obviously, the flow structure passing though the hole of the ballute for the towed and uniform freestream cases will differ because the total pressure in the spacecraft wake is less than its freestream counterpart. For example, the ballute calculations for $D/D_{cs} = 4$ and for uniform freestream conditions produce a recirculation region due to the self-induced shock interactions for only the lowest altitude (100 km) case, with the recirculation region located between $x = 12.8$ and 20.1 m. For the same ballute in the spacecraft wake at 100 km (Fig. 20), the recirculation region is much large and is located between $x = -15.8$ and 20.4 m. Also, with the ballute in the spacecraft wake and its reduced total pressure, recirculation occurs at 105 km (see Fig. 4), with the recirculation region located between $x = -2.2$ and 14.5 m. No recirculation is evident for the towed ballute at a 110-km altitude (Fig. 21) and higher.

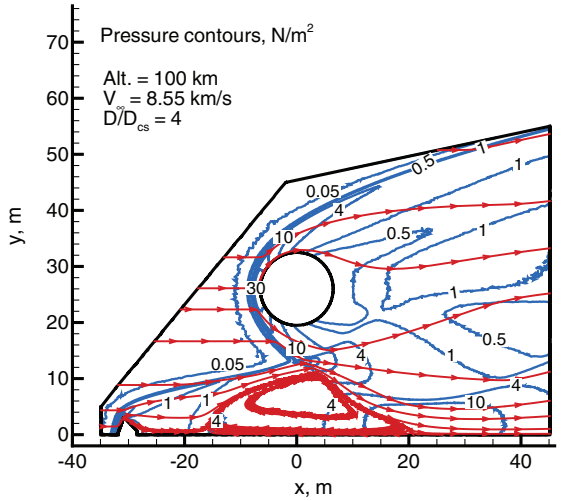

Fig. 20 Pressure contours and streamlines for a towed ballute at 100-km altitude.

Note that for the solutions in which a large recirculation region is present, the simulation time required for the recirculation region to assume a fixed location is significantly longer than the time required for the ballute surface distributions to achieve essentially constant values. As an example, the heating distribution for the towed ballute at 100 km (Fig. 19) experiences essentially the same heating rate distribution at 37 ms as it does at 75 ms, but the axial extent of the recirculation region increased by 9 m during this time interval.

G. Towed Ballute Configuration that Produces Unsteady Flow

Results presented in the previous sections suggest that the flow environment for the baseline configuration (D/D_{cs}) is steady based on the present time accurate simulations, with the caveat that they are time-averaged results. The stable aspect of the findings has also been confirmed by the experimental investigation of Rasheed et al. [9], where tests were performed in the California Institute of Technology T5 hypervelocity shock tunnel. Furthermore, the study of Rasheed et al. [9] also briefly examined a configuration where the flow was unsteady when the hole of the ballute was completely blocked by the use of an aluminum disk. A less dramatic approach was examined in the current investigation by selecting a configuration such that the spacecraft's shock impinged on the ballute's bow shock at a location in front of the ballute. The configuration selected was a ballute with a diameter ratio of 2 (ring diameter D equals 26 m and toroidal cross-sectional diameter D_{cs} equals 13 m) and the same separation distance (28.46 m) between ballute and spacecraft as the one shown in Fig. 4. With the combination of additional blockage due to the reduction in the size of the ballute's hole and the direct shock impingement on the ballute, the potential for an unsteady flow environment is greatly enhanced.

Figures 22–24 present results showing that the flow is unsteady for the problem just described. Even though the numerical simulation was preset to do time averaging to reduce the statical scatter, the unsteady aspects of the flow were sufficiently active to prevent the simulation from establishing a large sample for the steady-state result; that is, the DS2V program resets the time-averaged sample automatically if the fluctuating number of simulated molecules changes by more than a specified number of standard deviations. Instead of being able to generate typically tens of thousands of time-averaged samples, the program automatically resets the time-averaged results for a much smaller and random number of samples. Consequently, the results shown in Figs. 22–24 are for small time-averaged samples (Δtime); the specific simulation time intervals are included in Fig. 23.

A large recirculation region at a simulation time of 42.4 ms is evident in Fig. 24, where pressure contours and streamlines are displayed. The size of this region is such that it extends forward to a location on the afterbody of the spacecraft, a location where the

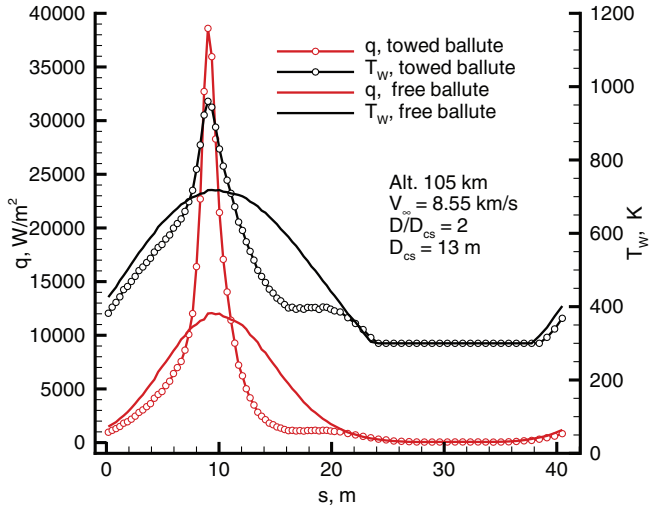

Fig. 22 Comparison of heating rate and radiative equilibrium wall temperature distributions for a towed configuration that produces unsteady flow (time = 42.4 ms) with that for steady flow about the same ballute at uniform freestream conditions.

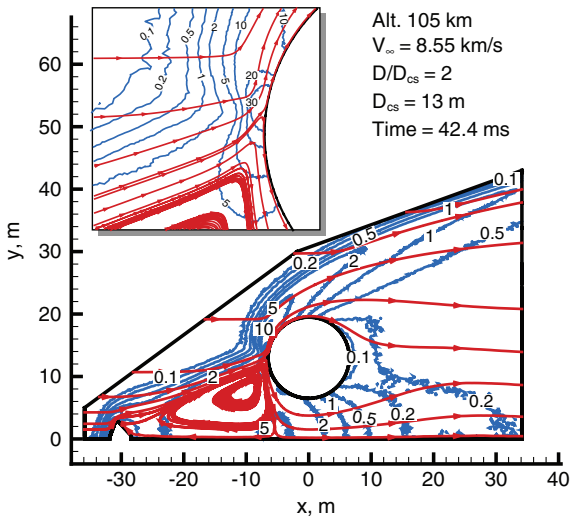

Fig. 24 Pressure contours and streamlines for unsteady results at simulation time = 42.4 ms. Results time averaged over the last 0.84 ms with 423 samples—sampling cells had approximately 80 simulated molecules per cell.

spacecraft radius is 2.45 m. The total extent of the recirculation region is 24.8 m (from −30.2 to −5.4 m). The flow configuration shown in Fig. 24 changes with time as is evident in Fig. 23, which shows both the location and peak heating rate values at selected times during the simulation. The peak heating locations move with time, where the excursions for the results presented cover a surface length s of about 0.9 m or about 8 deg. The changes in surface heating rate and wall temperature distributions, with respect to the corresponding ballute exposed to uniform freestream conditions, are given in Fig. 22, where the unsteady results are for a simulation time of 42.4 ms. The heating rate augmentation due to the shock interactions for the 42.4-ms simulation is 3.3 with respect to the steady uniform flow situation. The corresponding increase in the radiative equilibrium wall temperature is about 250 K. The impact of the shock interaction on pressure distribution is qualitatively similar to that for the heating, with an augmentation factor of 3.7 and a maximum surface pressure of 48 N/m^2. Note that the qualitative features of the surface heating rate distributions resulting from shock–shock interactions are in agreement with the DSMC study reported in [17], where the DSMC method was shown to give good agreement with experimental measurements, performed in a low-density Mach 10 wind tunnel, for shock structure (density and translational and rotational temperature profiles) and surface heating for Edney [18] type IV and type III shock–shock interactions.

In an effort to better characterize the nature of the unsteady flow (is the flow periodic, for example), the simulation was run for a longer time. Results for the longer run time showed that the time intervals for which the DS2V program was automatically resetting the samples were becoming larger. Eventually, at a simulation time of approximately 117 ms, the flow either became steady or the unsteady aspects were sufficiently small to avoid triggering the sample reset. Consequently, a time-averaged sample was generated (116.6 to 137.2 ms, 10,300 samples), and the results are similar to that previously discussed for the unsteady phase of the simulation. Figure 25 presents the large sample, time-averaged surface results for heating rate, pressure, and skin friction, in which the peak heating rate occurs at s = 8.5 m.

The localized augmentations in heating and pressure experienced by the ballute and the significant increase in afterbody heating and pressure experienced by the spacecraft are certainly undesirable events that hopefully can be avoided with proper attention to mission requirements and design issues. Unlike the current spacecraft-ballute configuration, which was fabricated to produce shock–shock

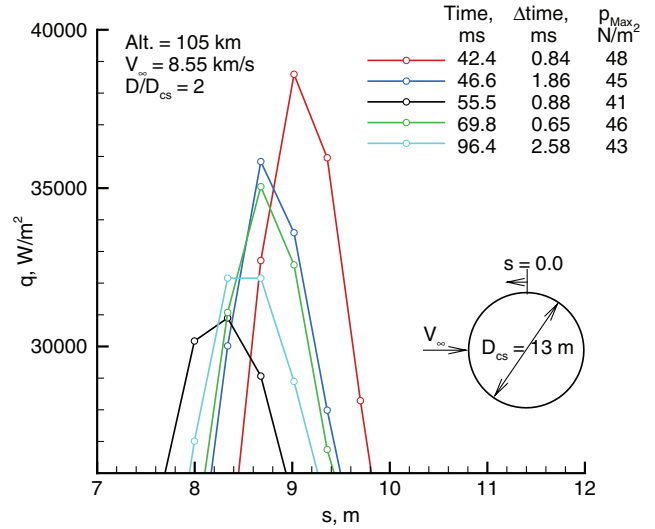

Fig. 23 Location and magnitude of maximum heating rates for unsteady flow about a towed ballute and the corresponding maximum surface pressures for different simulation times (Δtime denotes the interval for time averaging).

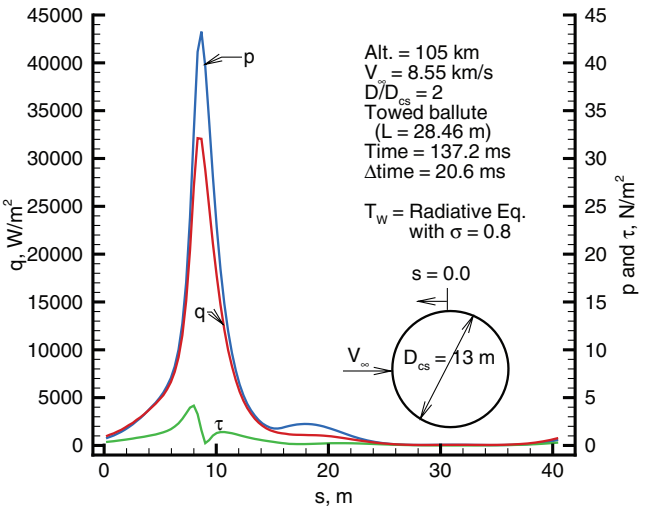

Fig. 25 Towed ballute surface distributions ("steady" results) for a simulation time = 137.2 ms. Results time averaged over the last 20.6 ms.

interactions that directly impacted the ballute, it appears that there should be a range of configurations, such as the baseline considered herein, for which the consequences of shock interactions and unstable flows can be negated.

IV. Conclusions

A computational study of hypersonic flow over a toroidal ballute and two bodies in tandem (the toroidal ballute towed by a spacecraft) is made by using the DSMC method. The computations are made for Earth entry conditions by using a 5-species reacting air model. Simulations were made for altitudes of 200–100 km, freestream velocities of 7–14 km/s, and toroidal ballute configurations in which the toroid ring diameter D to toroid cross-sectional diameter (a constant $D_{cs} = 13$ m) included values of 4, 3, and 2. The baseline toroidal ballute configuration ($D/D_{cs} = 4$) is one that has been used previously for Titan aerocapture studies. Results of the simulations show that the flow environment for the various elements of a towed ballute varies from free molecular to continuum conditions, with significant thermal and chemical nonequilibrium. Variations of drag and heating coefficients as a function of rarefaction are presented. A description of the flow structure is provided and also an explanation of how it is affected by shock interactions produced solely by the ballute and those resulting from the two body combination of a spacecraft and a towed ballute.

Significant findings of the present investigation are as follows: 1) of the isolated elements examined, tethers experienced the highest heating rates; 2) the towed ballute when using the baseline separation distance between spacecraft and ballute experienced the same surface distributions for heating rate, pressure, and skin friction as those for the isolated (uniform freestream flow) ballute, and consequently the same drag; and 3) a towed ballute configuration selected so that the spacecraft shock impinged directly on the ballute produced shock–shock interactions and an initially unsteady and large recirculation region, resulting in adverse aerothermodynamic loads for both the ballute and the aft end of the spacecraft.

References

[1] Jahemenko, I. M., "Ballute Characteristics in the 0.1 to 10 Mach Number Speed Range," *Journal of Spacecraft and Rockets*, Vol. 4, No. 8, 1967, pp. 1058–1063.

[2] Guy, L. D., "Structural and Decelerator Design Options for Mars Entry," *Journal of Spacecraft and Rockets*, Vol. 6, No. 1, 1969, pp. 44–49.

[3] McRonald, A. D., "A Light-Weight Inflatable Hypersonic Drag Device for Planetary Entry," AIAA Paper 99-0422, 1999.

[4] Hall, J. L., and Le, A. K., "Aerocapture Trajectories for Spacecraft with Large, Towed Ballutes," AAS Paper 01-235, Feb. 2001.

[5] Miller, K. L., Gulick, D., Lewis, J., Trochman, B., Stein, J., Lyons, D. T., and Wilmoth, R. G., "Trailing Ballute Aerocapture: Concept and Feasibility Assessment," AIAA Paper 2003-4655, July 2003.

[6] Gnoffo, P. A., and Anderson, B. P., "Computational Analysis of Towed Ballute Interactions," AIAA Paper 2002-2997, June 2002.

[7] Anderson, B. P., "Computational Continuum and Rarefied Flow Results For Ballute Applications," AIAA Paper 2004-0292, Jan. 2004.

[8] Hornung, H. G., "Hypersonic Flow Over Bodies in Tandem and Its Relevance to Ballute Design," AIAA Paper 2001-2776, June 2001.

[9] Rasheed, A., Fujii, K., Hornung, H. G., and Hall, J. L., "Experimental Investigation of the Flow Over a Toroidal Aerocapture Ballute," AIAA Paper 2001-2460, June 2001.

[10] Bird, G. A., *Molecular Gas Dynamics and the Direct Simulation of Gas Flows*, Clarendon, Oxford, England, U.K., 1994.

[11] Bird, G. A., *Visual DSMC Program for Two-Dimensional and Axially Symmetric Flows, The DS2V Program User's Guide*, Ver. 2.1, http://gab.com.au [retrieved Nov. 2003].

[12] Borgnakke, C., and Larsen, P. S., "Statistical Collision Model for Monte Carlo Simulation of Polyatomic Gas Mixture," *Journal of Computational Physics*, Vol. 18, No. 4, 1975, pp. 405–420.

[13] Bird, G. A., "The DS2V/3V Program Suite for DSMC Calculations," *Rarefied Gas Dynamics, 24th International Symposium*, edited by M. Capitelli, Vol. 762, American Inst. of Physics, Melville, NY, 2005, pp. 541–546.

[14] Moss, J. N., and Bird, G. A., "Direct Simulation Monte Carlo Simulations of Hypersonic Flows with Shock Interactions," *AIAA Journal*, Vol. 43, No. 12, 2005, pp. 2565–2573; also AIAA Paper 2004-2585, June 2004.

[15] Moss, J. N., Bird, G. A., and Markelov, G. N., "DSMC Simulations of Hypersonic Flows and Comparison With Experiments," *Rarefied Gas Dynamics, 24th International Symposium*, edited by M. Capitelli, Vol. 762, American Inst. of Physics, Melville, NY, 2005, pp. 547–552.

[16] Jacchia, L. G., "Thermospheric Temperature, Density, and Composition: New Models," Smithsonian Astrophysical Observatory, Special Rept. 375, Cambridge, MA, March 1977.

[17] Moss, J. N., Pot, T., Chanetz, B., and Lefbvre, M., "DSMC Simulations of Shock/Shock Interactions: Emphasis on Type IV Interactions," *Proceedings of the 22nd International Symposium on Shock Waves*, Vol. 2, Univ. of Southampton, Southampton, U.K., 2000, pp. 1337–1342.

[18] Edney, B., "Anomalous Heat Transfer and Pressure Distributions on Blunt Bodies at Hypersonic Speeds in the Presence of an Impinging Shock," Flygtekniska Forsoksanstalten (The Aeronautical Research Institute of Sweden), Stockholm, Rept. 115, 1968.

A. Ketsdever
Associate Editor